

Excess Adsorption of Helium in Extremely Narrow Slit Pores

Tomonori Ohba

Received: 3 April 2014 / Accepted: 14 August 2014 / Published online: 5 September 2014
© Springer Science+Business Media New York 2014

Abstract Wave functions of quantum helium in narrow slit pores are strongly restricted; as such, quantum helium condensed in narrow slit pores displays different behaviors from that in bulk. Herein, we report the densities of helium adsorbed on carbon surfaces and in carbon slit pores with average pore widths of 0.7, 0.9, and 1.1 nm at 2–5 K. The density of adsorbed quantum helium in the 0.7-nm slit pores was significantly higher than those in the larger slit pores and bulk. The average layer density of helium in the 0.7-nm pores was also significantly higher than those in the larger slit pores, suggesting solid-like structure formation even under helium vapor condition. The highly dense state of helium in narrow slit pores is due to strong attractive potential effects in such slit pores.

Keywords Quantum helium · Solid-like condensation · Adsorption · Carbon slit pores

1 Introduction

Helium is the most studied quantum fluid, characterized by its weak interatomic interaction and light mass, and exhibits unique quantum behaviors at low temperatures such as superfluidity and λ -transition at 2.2 K. The quantum behavior of a molecule can be evaluated using the thermal de Broglie wavelength, defined as $\lambda_{dB} = (h^2/2\pi mk_B T)^{1/2}$, where h , m , k_B , and T are the Planck constant, mass of the atom, Boltzmann constant, and temperature, respectively. The λ_{dB} of helium is 0.05 nm at 300 K. Considering that the molecular size of helium is ≈ 0.29 nm, the interatomic distances are significantly greater than the λ_{dB} at 300 K. Quantum effects

T. Ohba (✉)
Graduate School of Science, Chiba University, 1-33 Yayoi, Inage, Chiba 263-852, Japan
e-mail: ohba@pchem2.s.chiba-u.ac.jp

are therefore trivial at room temperature. However, at 4.2 K, when helium-4 becomes a liquid at an ambient pressure, the λ_{dB} (0.43 nm) is larger than the molecular size (0.29 nm). Thus, evaluating quantum effects is essential to understanding molecular behaviors at very low temperatures.

Pores provide microscopic space limitation for quantum molecules [1–6]. Hence, typical condensate wave functions are likely to be inappropriate for slit pores. The superfluidity of helium in slit pores was reviewed by Reppy [7]. Helium in relatively large slit pores behaved similarly to bulk helium. However, the temperature of the superfluid transition was lower because the coverage of a helium “film” was smaller. In addition, the density of adsorbed helium, which is defined as the amount of adsorbed helium per unit pore volume, in the large slit pores was significantly reduced. Wada et al. reported low-dimensional helium behaviors in various pore systems [8, 9]. The temperature of superfluid transition for sub-monolayer films decreased with increasing pore widths [8]. Superfluid transition in different dimensional 3-nm pores was strongly dependent on the pore connectivity [9], highlighting the strong influence of narrow slit pores on quantum behaviors. Therefore, quantum helium confined in narrow slit pores should show unique behaviors relative to those observed in bulk helium and large pores. Herein, we investigate helium quantum effects in extremely narrow slit pores of activated carbon fibers (ACFs) at 2–5 K and on carbon surfaces of Grafoil via helium adsorption measurements and path-integral Monte Carlo simulations.

2 Experimental and Simulation Procedures

The ACFs (Adall Co.) studied herein have relatively large slit pore volumes and uniform slit pores, as evaluated by α_S -analysis of the N_2 adsorption isotherms measured at 77 K. The nanospaces between the graphitic units are termed as slit pores. We used three types of ACFs with different slit pore widths of 0.7, 0.9, and 1.1 nm, referred as ACF07, ACF09, and ACF11, respectively. Helium adsorption isotherms were measured on an in-house built volumetric adsorption apparatus equipped with a superconducting quantum interference device (MPMS XL, Quantum Design Co.) to control the temperature. Prior to measurements, the ACFs were degassed at 373 K below 1 mPa for at least 2 h. The helium adsorption studies of the nanoporous carbon samples (ACFs) and non-porous carbon surface (Grafoil) were conducted at 2–5 K.

Path-integral Monte Carlo simulations were performed to evaluate the adsorption mechanism of quantum helium in the carbon slit pores. The carbon slit pores were composed of two parallel graphitic units and the gap between those graphitic units formed a slit pore. A slit pore width is defined as the distance between two graphitic surfaces. The method has been widely used for evaluating various physical properties of normal liquid, superfluid, and condensed helium [10, 11]. The path-integral partition function is described by ring polymers, consisting of polymer beads representing particles with a known mass, as follows:

$$P(N) = \frac{1}{\Xi} e^{\beta\mu N} \frac{V^N}{N!} \left(\frac{2\pi m P k_B T}{h^2} \right)^{3NP/2} \times \exp \left[-\beta(U^{int} + U^{ext}) \right] \quad (1)$$

where β , μ , V , N , m , and P denote $1/k_B T$, chemical potential, volume of the unit cell, number of helium atoms, mass of an atom, and polymer beads number. Interaction between the polymer beads (U^{int}) and interatomic interactions between helium atoms and helium atom–carbon atom (U^{ext}) are given by:

$$U^{int} = \sum \frac{mP}{2\beta^2\hbar^2} (r_{i+1}^j - r_i^j)^2 \text{ and } U^{ext} = \sum \frac{\Phi(r_i^j - r_i^k)}{P}. \quad (2)$$

Here, r_i^j and $\Phi(r_i^j - r_i^k)$ respectively refer to the position of the i -th polymer bead in the j -th atom and the Lennard–Jones potential between the i -th polymer beads of the j -th and k -th atoms for helium–helium and helium–carbon atoms. Lorentz–Berthelot mixing rules were used to calculate interatomic interactions between helium and carbon atoms. The calculation method is based on a quantum system obtained by replacing the classical partition function with the quantum partition function. Further details of the calculation methods are reported elsewhere [10–15]. The path-integral and classical Monte Carlo simulations were performed for evaluating the structure of adsorbed helium and corresponding behavior in the carbon slit pores. The number of polymer beads used in the path-integral and classical Monte Carlo simulations were 50 and 1, respectively. The collision diameter (σ_{He}) and interaction potential (ε_{He}/k_B) were 0.2556 nm and 10.22 K, respectively [16]. The collision diameter (σ_C) and interaction potential (ε_C/k_B) of carbon were 0.3416 nm and 30.14 K, respectively [17, 18]. The parameters also described behaviors of molecules adsorbed on the activated carbon samples. The interatomic interactions were calculated using the above equations that accounted for interactions between the polymer beads of two different atoms. A spring connecting a bead and the neighboring bead provides the harmonic oscillator potential. The harmonic potential is due to the quantum behavior of helium. The interaction potential between a helium atom at an adsorption site and a carbon slit pore was evaluated prior to conducting the path-integral canonical Monte Carlo simulation using the above interaction potential because the calculation time could be efficiently reduced. The graphitic unit was composed of five graphene layers each of $\approx 5 \times 5 \text{ nm}^2$, affording sufficiently large graphitic units to evaluate the adsorption potential of a helium atom in the carbon slit pores [19]. A helium atom was positioned at the center of the graphene layers and the helium adsorption potentials at various distances from the surface of a graphitic unit were calculated to obtain the interaction potential between a helium atom and a carbon slit pore. The carbon–carbon distance in a graphene layer and graphene layer distance at 2–5 K were assumed to be constant (0.142 and 0.335 nm, respectively).

Validation of the simulation was conducted by assessing the λ -transition-like heat-capacity change of quantum helium in bulk; λ -transition was observed at 2.5 K in the simulation, roughly agreeing with the temperature of λ -transition in liquid helium at 2.2 K. The simulation methodology employed was the same as the typical canonical Monte Carlo simulation except for the interatomic potential functions. Molecular numbers of helium in the 0.7-, 0.9-, 1.1-, 1.5-, 2.0-, and 3.0-nm pores were 540, 447, 530, 720, 960, and 1440, respectively, and defined by the same adsorbed densities evaluated from the adsorption isotherms for the 0.7–1.1-nm pores. The simulation

involves three types of random movements: displacement, creation, and deletion of an atom in Metropolis sampling. A cubic unit cell of $5 \times 5 \times 5 \text{ nm}^3$ was used for the simulations and the calculation cycle was 1×10^6 steps at each equilibrium pressure.

3 Results and Discussion

The nanoporous structures were evaluated from N_2 adsorption studies performed at 77 K, as shown in Fig. 1 and Table 1. ACFs have relatively large slit pore volumes and uniform slit pores. Pore width is defined as the slit width between carbon surfaces. The 0.7-, 0.9-, and 1.1-nm pores of the ACFs approximately correspond to 2.2-, 3.1-, and 3.9-layer thickness of classical helium. Herein, the size of classical helium is 0.29 nm, evaluated from a constant interatomic distance in the Lennard–Jones model. However, an additional layer could be formed using the classical Monte Carlo simulations, as mentioned later.

Figure 2 shows the helium adsorption isotherms in carbon nanopores and on carbon surfaces. Condensation of helium in the nanopores can be observed at the extremely low pressure regions, whereas slight adsorption of helium was observed onto the carbon surfaces within the same pressure region. Temperature-dependent adsorbed amounts behaviors were observed in the 1.1-nm pores. In contrast, the helium adsorp-

Fig. 1 N_2 adsorption isotherms of ACFs and Grafoil at 77 K (Color figure online)

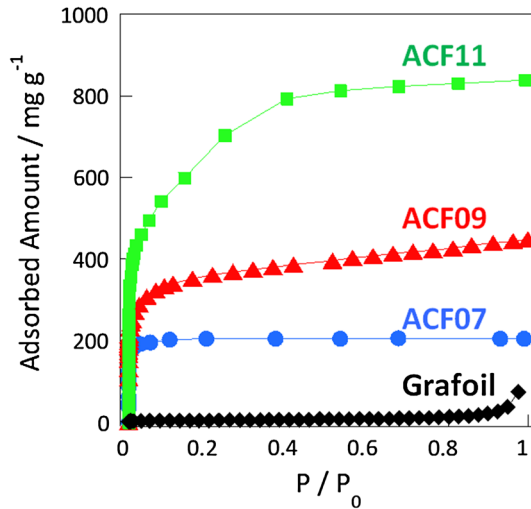


Table 1 Pore properties of ACFs and Grafoil evaluated from α_S -analysis of the N_2 adsorption isotherms

	Surface area ($\text{m}^2 \text{ g}^{-1}$)	Pore volume (mL g^{-1})	Pore width (nm)
ACF07	777	0.25	0.65
ACF09	1140	0.49	0.89
ACF11	1648	0.91	1.13
Grafoil	12	0.00	–

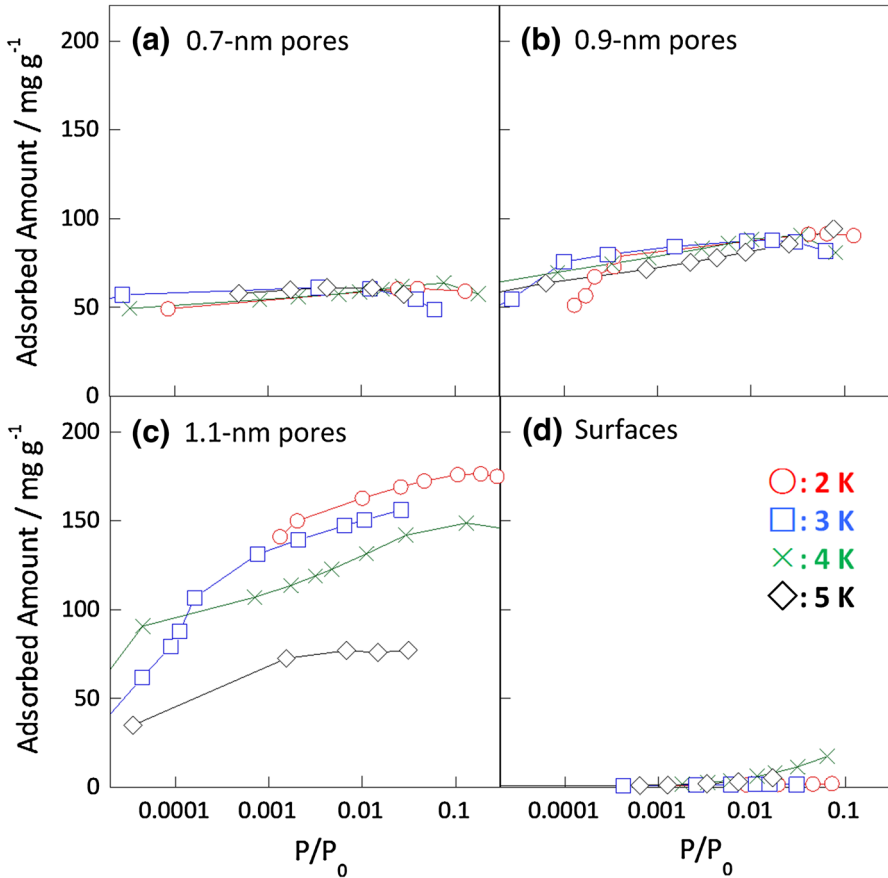
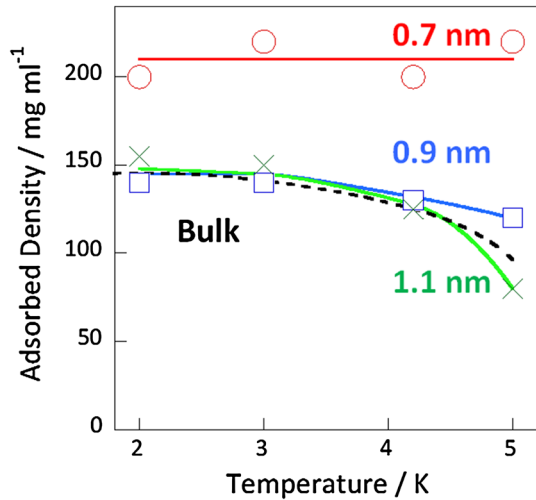


Fig. 2 Dependency of adsorbed helium density on pore width. Helium adsorption isotherms measured at 2–5 K **a–c** in the carbon slit pores (0.7–1.1 nm) of the ACFs and **d** carbon surfaces. P_0 is defined as the saturated vapor pressure of helium (Color figure online)

tion amounts in the 0.7- and 0.9-nm pores were independent of temperature in the range of 2–5 K.

The adsorbed helium density values in the slit pores at varying temperatures were obtained from the corresponding adsorption isotherms and pore volumes, as shown in Fig. 3. The adsorbed helium densities in the 0.9- and 1.1-nm pores were similar to the bulk density values, as reported elsewhere [20]. More specifically, the adsorbed density values in the 0.9- and 1.1-nm pores at 5 K were respectively higher and lower than the bulk density values, indicating that helium at 5 K was strongly and loosely adsorbed in the 0.9- and 1.1-nm pores. Surprisingly, the adsorbed density in the 0.7-nm pores at varying temperatures was approximately 210 mg mL^{-1} , corresponding to an increase of $>40\%$ relative to the other obtained density values. In summary, the adsorbed density was mostly independent of the temperatures studied herein. The high adsorbed densities are due to the formation of a solid helium layer on the pore surface, as discussed later.

Fig. 3 Adsorbed helium densities in the carbon slit pores as a function of temperature (2–5 K) at $P/P_0 = 0.01$. Circle: 0.7-nm pores; square: 0.9-nm pores; times: 1.1-nm pores, and dashed line: bulk (Color figure online)



Path-integral and classical Monte Carlo simulations of helium in the 0.7–1.1-nm pores at 4 K were performed to investigate the behaviors of helium in the slit pores. Figure 4a shows snapshots of quantum helium in the slit pores; the layer numbers in the 0.7-, 0.9-, and 1.1-nm pores were not distinct. The polymer beads are loosely bound at low temperatures and thus, the atomic size and potential depth are larger and shallower than those of a classical helium atom. Figure 4b shows the distribution profiles of quantum and classical helium adsorbed in the slit pores, obtained from the snapshots in Fig. 4a. The distribution profiles clearly show that the layer numbers of adsorbed quantum helium were 2, 3, and 4 in the 0.7-, 0.9-, and 1.1-nm pores, respectively, whereas the layer numbers of classical helium were 3, 4, and 5 layers, respectively. The distribution of quantum helium was broad and the associated layer numbers were lower than those associated with classical helium. Quantum helium atoms at monolayer sites were more distant from carbon surfaces than classical helium atoms.

The average layer densities of helium or two-dimensional density were obtained from helium adsorption isotherms, surface areas, and the above estimated layer numbers of quantum helium in the 0.7-, 0.9-, and 1.1-nm pores (i.e., 2, 3, and 4, respectively). The layer numbers were consistent with the estimated layer numbers from the atomic size and average pore width: 2.2 layers in the 0.7-nm pores, 3.1 layers in the 0.9-nm pores, and 3.9 layers in the 1.1-nm pores. Figure 5 shows the temperature dependence of average layer densities of helium in slit pores, evaluated from the adsorbed densities in Fig. 3 and the layer numbers in Fig. 4. The average layer densities of helium were 11.7 and 7.4 atoms nm^{-2} for the 0.7- and 0.9-nm pores, respectively regardless of the temperature. The average layer densities in the 1.1-nm pores decreased with increasing temperatures from 7.4 to 3.5 atoms nm^{-2} . The density in the crystalline phase is larger than 7 atoms nm^{-2} , and the densities of adsorbed helium at the monolayer and second-layer sites on graphite were approximately 11.5 and 8 atoms nm^{-2} , respectively, as reported elsewhere [21–23]. The estimated helium

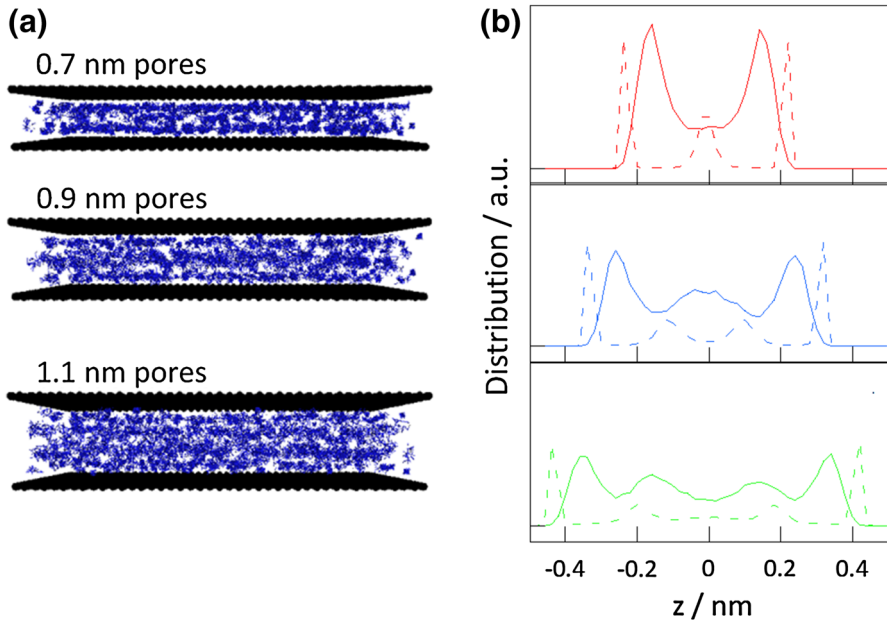
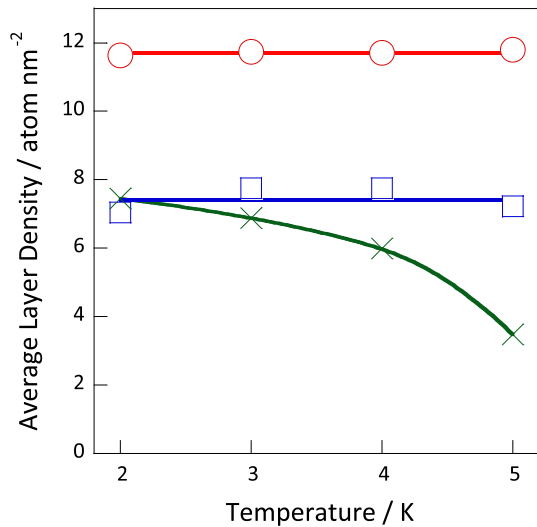


Fig. 4 **a** Snapshots of helium in the 0.7-, 0.9-, and 1.1-nm pores using path-integral Monte Carlo simulation. The *blue spheres* represent the polymer beads of a helium atom and *black surfaces* represent the carbon walls. **b** Helium distribution profiles in a pore using path-integral Monte Carlo simulation (*solid curves*) and classical Monte Carlo simulation (*dashed curves*). The intensities obtained from the classical Monte Carlo simulation were one-third of those obtained from the quantum Monte Carlo simulation. The pore center is at $z = 0$ (Color figure online)

Fig. 5 Average layer densities of helium adsorbed in the slit pores. *Circle*: 0.7-nm pores; *square*: 0.9-nm pores; and *times*: 1.1-nm pores (Colour figure online)



layer densities were 11.5, 10.3, 9.8 atoms nm⁻² for the 0.7-, 0.9-, and 1.1-nm pores, respectively. In the 0.7-nm pores, the helium layer density was consistent with the estimated value (monolayer density on graphite), suggesting crystalline structure formation in such narrow pores even at $P/P_0 = 0.01$ and 2–5 K. The densities in the 0.9-nm pores were lower than the estimated value (10.3 atoms nm⁻²) and the density on the second-layer site (8 atoms nm⁻²). Helium in the 0.9-nm pores was thus present in a relatively less dense state than that in the 0.7-nm pores, indicating that the helium structure was liquid-like. Temperature dependence of the average layer densities in the 1.1-nm pores is due to further loose structure formation. Therefore, helium in the 0.7-nm pores was solid-like under helium vapor condition, whereas that in the 0.9- and 1.1-nm pores was liquid-like.

4 Conclusion

In this study, the properties of quantum helium in carbon slit pores were assessed. The adsorbed helium densities in the 0.9- and 1.1-nm slit pores were similar to those of quantum liquid helium in bulk evaluated at 2–5 K. Additionally, the helium layer densities were smaller than that of solid-like helium. In contrast, higher adsorbed helium densities were observed in the 0.7-nm slit pores at 2–5 K. Moreover, the helium layer densities were similar to the density of solid-like helium on graphite under helium vapor condition. Thus, the excess dense state of quantum helium was observed in the extremely narrow slit pores, indicating the onset of an excess condensation effect in such narrow slit pores.

Acknowledgments I would like to thank Prof. Katsumi Kaneko from Shinshu University, Japan for valuable discussions. This research was supported by the Japan Society for the Promotion of Science (KAKENHI Grant No. 26706001) and Research Fellowships from the Futaba Electronics Memorial Foundation.

References

1. S. Bera, J. Maloney, L.B. Lurio, N. Mulders, Z.G. Cheng, M.H.W. Chan, C.A. Burns, Z. Zhang, *Phys. Rev. B* **88**, 054512 (2013)
2. R. König, F. Pobell, *Phys. Rev. Lett.* **71**, 2761 (1993)
3. M. Boninsegni, D.M. Ceperley, *Phys. Rev. Lett.* **74**, 2288 (1995)
4. J.J. Beenakker, V.D. Borman, S.Y. Krylov, *Chem. Phys. Lett.* **232**, 379 (1995)
5. Q. Wang, S.R. Challa, D.S. Sholl, J.K. Johnson, *Phys. Rev. Lett.* **82**, 956 (1999)
6. X. Zhao, S. Villar-Rodil, A.J. Fletcher, K.M. Thomas, *J. Phys. Chem. B* **110**, 9947 (2006)
7. J.D. Reppy, *J. Low Temp. Phys.* **87**, 205 (1992)
8. K. Shirahama, K. Kubota, S. Ogawa, N. Wada, T. Watanabe, *Phys. Rev. Lett.* **64**, 1541 (1990)
9. N. Wada, M.W. Cole, *J. Phys. Soc. Jpn.* **77**, 111012 (2008)
10. D.M. Ceperley, *Rev. Mod. Phys.* **67**, 279 (1995)
11. P. Sindzingre, M.L. Klein, D.M. Ceperley, *Phys. Rev. Lett.* **63**, 1601 (1989)
12. E.S. Hernández, M.W. Cole, M. Boninsegni, *J. Low Temp. Phys.* **134**, 309 (2004)
13. S.M. Gatica, G. Stan, M.M. Calbi, J.K. Johnson, M.W. Cole, *J. Low Temp. Phys.* **120**, 337 (2000)
14. M. Boninsegni, N. Prokof'ev, B. Svistunov, *Phys. Rev. Lett.* **96**, 105301 (2006)
15. Q. Wang, J.K. Johnson, J.Q. Broughton, *J. Chem. Phys.* **107**, 5108 (1997)
16. L. Firlej, B. Kuchta, *Colloids Surf. A* **241**, 149 (2004)
17. Y.F. Yin, B. McEnaney, T.J. Mays, *Carbon* **36**, 1425 (1998)
18. T. Ohba, H. Kanoh, *J. Phys. Chem. Lett.* **3**, 511 (2012)

19. T. Ohba, A. Takase, Y. Ohyama, H. Kanoh, *Carbon* **61**, 40 (2013)
20. R.J. Donnelly, C.F. Barenghi, *J. Phys. Chem. Ref. Data* **27**, 1217 (1998)
21. P. Whitlock, G. Chester, B. Krishnamachari, *Phys. Rev. B* **58**, 8704 (1998)
22. M. Bretz, J. Dash, D. Hickernell, E. McLean, O. Vilches, *Phys. Rev. A* **8**, 1589–1615 (1973)
23. R.E. Ecke, J.G. Dash, *Phys. Rev. B* **28**, 3738–3752 (1983)